PCCP

Accepted Manuscript

ROYAL SOCIETY OF CHEMISTRY

www.rsc.org/pccp

Cite this: DOI: 10.1039/c0xx00000x

www.rsc.org/xxxxxx

COMMUNICATION

Water-plasma-assisted synthesis of black titania spheres with efficient visible-light photocatalytic activity

Gasidit Panomsuwan,*[a] Anyarat Watthanaphanit,[bc] Takahiro Ishizaki[ae] and Nagahiro Saito[bcde]

Received (in XXX, XXX) Xth XXXXXXXXX 20XX, Accepted Xth XXXXXXXXX 20XX

DOI: 10.1039/b000000x

Black titania spheres (H-TiO_{2-x}) were synthesized *via* a simple green method assisted by water plasma at low temperature and atmospheric pressure. The *in situ* production of highly energetic hydroxyl and hydrogen species from water plasma are the prominent factors for the oxidation and hydrogenation reactions during the formation of H-TiO_{2-x}, respectively. The visible-light photocatalytic activity toward dye degradation of H-TiO_{2-x} can be attributed to the synergistic effect of large surface area, visible-light absorption, and existence of oxygen vacancies and Ti^{3+} sites.

Titania (TiO_2) has long been regarded as one of the most promising photocatlysts for the global-environmental cleaning and production of hydrogen by utilizing solar radiation, owing to its long-term stability, inexpensiveness, availability, and non-toxicity toward both human beings and the environment.[1] However, TiO_2 photocatalyst is virtually inactive within the visible-light region (about 43% of solar radiation) due to its wide band gap, typically ~3.2 eV for anatase and ~3.0 eV for rutile.[2] A massive recombination of photogenerated electron-hole pairs is also one of the undesirable phenomenon that substantially diminishes the photocatalytic efficiency of TiO_2.[3] To address these particular issues, considerable recent research effort of TiO_2 photocatalysts has been intensively conducted on the basis of three strategies: i) extending the excitation wavelength toward the visible-light region, ii) inhibiting the recombination of photogenerated electron-hole pairs by enhancing charge separation, and iii) increasing the surface area and quantity of active sites.[4–16] So far, these strategies have been achieved by modifying TiO_2 through several rational designs and engineering approaches, such as doping non-metal atoms (*e.g.*, N, B, S, and F),[4–7] decorating the surface with noble-metal nanoparticles (*e.g.*, Au, Pt, Ag, and Pd),[8–11] and compositing with carbonaceous substances (*e.g.*, carbon nanotubes, graphene, and fullerenes).[12–14] Most recently, Chen *et al*. reported that hydrogenated black TiO_2 (H-TiO_{2-x}) revealed outstanding photocatalytic activity for the degradation of organic dye pollutants and the production of hydrogen from water splitting under solar irradiation.[17] The existence of oxygen vacancies and Ti^{3+} sites has been proven as a key role in significantly enhancing visible-light photocatalytic activity of H-TiO_{2-x}. This finding has presented the most important breakthrough in the TiO_2 photocatalysis research community. Thenceforth, the research and development on highly active TiO_2 visible-light photocatalysts through defect engineering have progressed rapidly.[18–35] Although numerous research efforts have been devoted to this exciting field, the method for synthesizing H-TiO_{2-x} has mostly relied on the reduction of pristine stoichiometric TiO_2 (reducing Ti^{4+} to Ti^{3+}) by thermal treatment under hydrogen or oxygen-depleted conditions, chemical vapor deposition, and high-energy particle bombardment (*e.g.*, electron, argon, and hydrogen plasma).[17–35] These methods inevitably involve high processing temperatures (> 500 °C), a vacuum system, long processing times, and multi-step processes, which are major barriers for practical implementation. Therefore, it is very challenging and desirable to draw up new prospects for the synthesis of H-TiO_{2-x}.

Herein, we have developed a simple green method assisted by water plasma for the synthesis of H-TiO_{2-x} at low temperature and atmospheric pressure. Plasma generated inside liquid water is an intriguing source and an energetically challenging reaction for the *in situ* production of highly reactive species, radicals, atoms, and ions due to the low dissociation energy of water.[36] In brief, the plasma was generated in liquid water between a pair of metallic Ti electrodes by applying microsecond bipolar high-voltage pulses with high frequency (Fig. S1† and S2†). The optical emission spectrum clearly shows the emission peaks attributed to Ti I (neutral), Ti II (single-charged ions), hydrogen, hydroxyl radicals, and atomic oxygen (Fig. 1). The generation of hydroxyl radicals is very important for the oxidation process due to its highest oxidation potential in comparison with other oxidative species.[37] In addition, highly kinetic energy and fast diffusion of H atoms play essential role in the hydrogenation reaction.[40] Once the water plasma was generated, the surfaces of Ti electrodes were predominantly bombarded with OH^- and O_2^- because the negative ion species were dominantly localized inside the plasma region,[39] resulting in the electrode surface oxidation. Subsequently, the continuous bombardment by highly energetic atomic and molecular species from the water plasma could create a number of local hot spots on the oxidized electrode surface due to the Joule heating effect. The molten particles came off the electrode surface and then formed a spherical shape due to the effect of surface tension. We hypothesize that the molten particles were readily re-oxidized in the plasma phase and subsequently hydrogenated at/near the plasma-liquid interface before ejecting to the liquid phase. A dramatic quenching of the molten particles

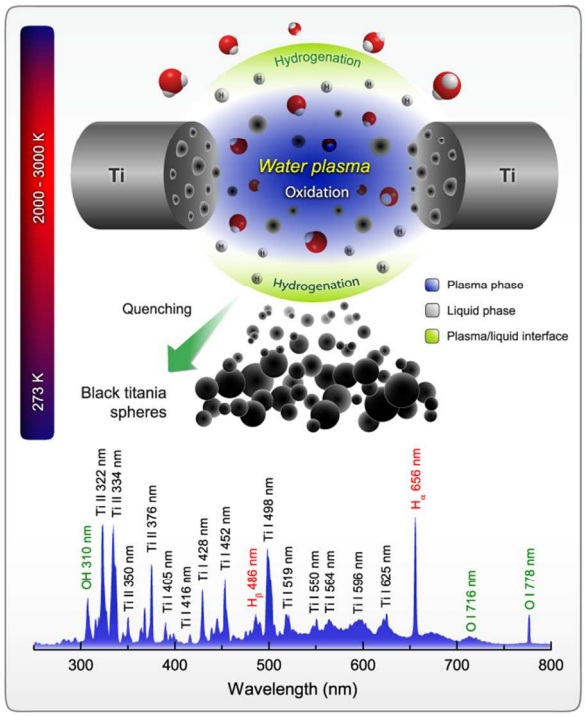

Fig. 1. The proposed formation mechanism of H-TiO_{2-x} spheres assisted by water plasma and the corresponding optical emission spectrum of water plasma generated through Ti electrodes.

in the liquid phase resulted in the freeze of metastable defects and disordered surface. The proposed formation mechanism of H-TiO_{2-x} spheres is depicted in Fig. 1. The morphological feature, structural properties, chemical bonding state, and visible-light photocatalytic activity of H-TiO_{2-x} spheres were investigated and discussed. Commercial TiO_2 (Aeroxide P25) was concurrently investigated as a benchmark for comparison throughout this study.

Diffuse reflectance spectra of P25 and H-TiO_{2-x} are shown in Fig. 2. As expected, the P25 shows a sharp absorption edge at a wavelength of 370 nm. In contrast, the H-TiO_{2-x} possesses a strong and broad absorption in the visible-light range throughout the near-infrared regions, while its absorption edge occurs at a longer wavelength of 440 nm. The band gap of H-TiO_{2-x} estimated from the Tauc plot is approximately 2.18 eV, which is much narrower than that of P25 (*ca*. 3.02 eV) (Fig. S3†). This result suggests that the H-TiO_{2-x} is more active in the visible-light and infrared regions with a narrower intrinsic band gap compared to those of P25. The visible-light absorption and the black color of H-TiO_{2-x} are attributed to the existence of oxygen vacancies and Ti^{3+} sites.[21,29,30] The black color of H-TiO_{2-x} was nearly unchanged for several months under ambient conditions, confirming the stability of defects in H-TiO_{2-x}.

The scanning electron microscopy (SEM) and bright-field transmission electron microscopy (BF-TEM) images of H-TiO_{2-x} are displayed in Fig. 3a and 3b, respectively. The H-TiO_{2-x} particles have a perfect spherical shape with a broad size distribution ranging from several-hundred nanometers to a few micrometers (Fig. S4†). High-resolution TEM images were also

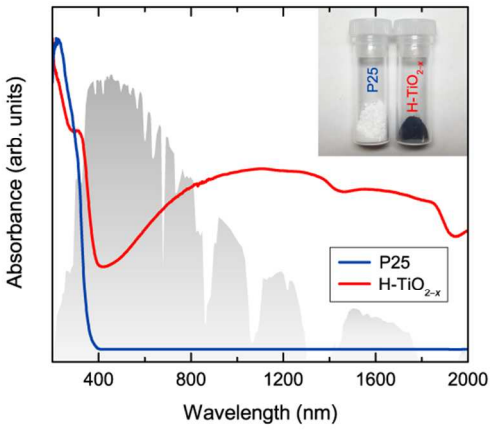

Fig. 2 Diffuse reflectance spectra of P25 and H-TiO_{2-x} (UV light: < 400 nm, visible light: 400–800 nm, infrared light: > 800 nm). The spectrum of solar radiation is displayed in the background for comparison. The inset shows the color of P25 (white) and H-TiO_{2-x} (black).

investigated at the bulk and surface regions of H-TiO_{2-x}. At the bulk region, obvious lattice fringes corresponding to the (110) plane of the rutile phase can be seen (Fig. 3c). On the contrary, a disordered structure and amorphous phase are observed at the surface of H-TiO_{2-x} (Fig. 3d). This result suggests that the H-TiO_{2-x} exhibits good crystallinity in bulk with a disordered surface. To gain an insight into the morphological feature of H-TiO_{2-x}, the specific surface area, pore volume, average pore diameter, and pore-size distribution were evaluated using nitrogen adsorption-desorption isotherms (Fig. S5a†). The specific surface area of H-TiO_{2-x} calculated using the Brunauer-Emmett-Teller (BET) method is about 120 $m^2\ g^{-1}$, which is almost three times greater than that of P25 (43 $m^2\ g^{-1}$). The larger specific surface area of H-TiO_{2-x} is most likely due to the rough adsorbing surface and the overlapping of a broad range of particle

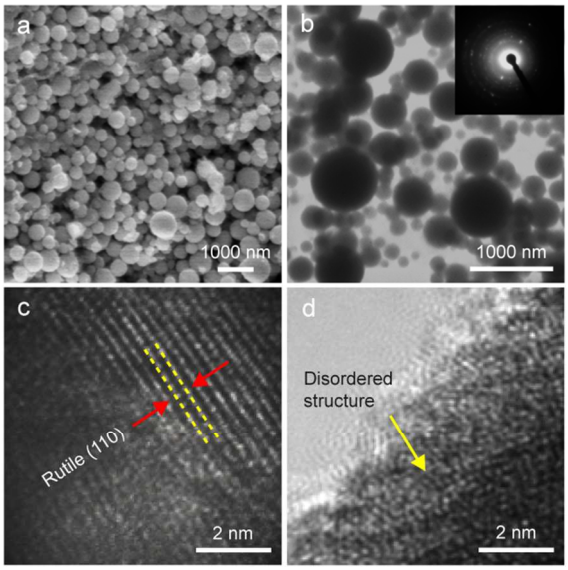

Fig. 3 (a) SEM image and (b) bright-field TEM image of H-TiO_{2-x}. HRTEM images of H-TiO_{2-x} at (c) bulk and (d) surface regions. The inset in (b) shows the corresponding selected area electron diffraction pattern.

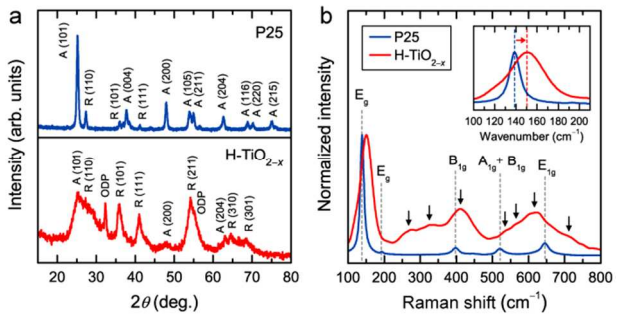

Fig. 4 (a) XRD patterns of P25 and H-TiO_{2-x}. The rutile (JCPDS No. 21-1276), anatase (JCPDS No. 21-1272), and oxygen-deficient phases[40] are denoted as R, A, and OPD, respectively. (b) Raman spectra of P25 and H-TiO_{2-x}. The inset shows the enlarged view of the main E_g peak of P25 and H-TiO_{2-x}.

sizes.[40] Therefore, the H-TiO_{2-x} would have more sites accessible for adsorption of the organic dyes in comparison with P25. The pore volume, average pore diameter, and pore size distribution of both P25 and H-TiO_{2-x} were also determined using the Barrett-Joyner-Halenda (BJH) method and shown in Fig. S5b† and Table S1†.

X-ray diffraction (XRD) patterns of P25 and H-TiO_{2-x} are shown in Fig. 4a. The P25 reveals the diffraction peaks corresponding to both anatase and rutile phases without other phases. The XRD pattern of H-TiO_{2-x} is composed of the mixture of rutile, anatase, and oxygen-deficient phases (*e.g.*, $Ti_{10}O_{19}$ Ti_5O_9, and Ti_3O_5).[40] The fraction of rutile phase is quite higher than that of anatase in H-TiO_{2-x}, which may be due to the high temperature in the plasma region. It has been reported that the anatase to rutile phase transformation in TiO_2 usually occurs at temperatures of > 600 °C.[43,44] A broadening of rutile and anatase diffraction peaks of H-TiO_{2-x} is possibly related to the existence of oxygen vacancies, which result in disorder-induced lattice strain and reduced crystallite size.[35] Further structural information was investigated using Raman spectroscopy (Fig. 4b). The Raman spectrum of P25 clearly shows six Raman-active modes of the anatase phase ($3E_g + 2B_{1g} + A_{1g}$).[45] Comparing the Raman spectra of P25 and H-TiO_{2-x}, three different features can evidently be observed. First, the Raman peaks of H-TiO_{2-x} are much broader than those of P25. Second, the Raman peaks of H-TiO_{2-x} occur at higher wavenumbers in comparison with those of P25. These two features are evidence that oxygen vacancies (Ti^{3+} sites) and/or structural disorder exist in the lattice structure of H-TiO_{2-x}.[24,27,32] The third feature is the presence of additional peaks (indicated as arrows in Fig. 4b), which are probably associated with the rutile and oxygen-deficient phases in H-TiO_{2-x}.[27,43]

X-ray photoelectron spectroscopy (XPS) was employed to elucidate the chemical bonding state and valence band maximum (VBM) of P25 and H-TiO_{2-x}. Apart from a very weak C 1s peak (284.5 eV) from carbon contamination, only the peaks related to titanium and oxygen are observed from the XPS survey spectra of P25 and H-TiO_{2-x}, (Fig. S6†). High-resolution XPS spectra Ti 2p and O 1s spectra for both samples are shown in Fig. 5a and 5b, respectively. As can be seen, the XPS Ti 2p spectrum of P25 is only composed of two peaks centered at 458.6 and 464.2 eV, which correspond to Ti $2p_{3/2}$ and Ti $2p_{1/2}$ peaks of Ti^{4+} in TiO_2, respectively. On the other hand, the XPS Ti 2p spectrum of H-TiO_{2-x} can be resolved into six peaks. In addition to the main sharp peaks of Ti^{4+} in TiO_2 (458.5 and 464.2 eV), two shoulder peaks at lower binding energies can also be detected on both Ti $2p_{3/2}$ (457.2 and 456.2 eV) and Ti $2p_{1/2}$ peaks (462.9 and 461.9 eV), which are associated with the presence of Ti^{3+} and Ti^{2+} species (Fig. 5a and Table S2†).[44,45] The $(Ti^{3+}+Ti^{2+})/Ti^{4+}$ ratios calculated from the corresponding XPS Ti 2p peak areas of H-TiO_{2-x} is found to be approximately 43%. The XPS O 1s spectra can be deconvoluted into three and four peaks for P25 and H-TiO_{2-x}, respectively (Fig. 5b). The main peak at 529.8 eV is assigned to the lattice oxygen in TiO_2 (Ti^{4+}–O), while the peak at a lower energy of 528.3 eV is associated with oxygen bonded to Ti^{2+} species (Ti^{2+}–O).[44,45] Two further peaks at higher binding energies of 531.1 and 532.2 eV are attributed to oxygen vacancies of TiO_2 (Ti^{3+}–O) and the presence of adsorbed oxygen or surface hydroxyl species, respectively.[44–46] The detailed deconvolutions of XPS Ti 2p and O 1s spectra are summarized in Table S2†. This result indicates that the surface of H-TiO_{2-x} contains more oxygen vacancies and Ti^{3+} species than that of P25. Furthermore, the valence band maximum (VBM) was determined by linear extrapolation of the peak to the baselines of the valence band XPS spectra (Fig. 5c). The VBM of P25 shows a band edge position at 2.04 eV below the Fermi energy, while that of H-TiO_{2-x} occurs at a binding energy close to the Fermi energy (0.83 eV) owing to the formation of a band tail above the VBM. The presence of a band tail state above the VBM of H-TiO_{2-x} is similar to several previous reports.[17,24,33] Combined with the band gap estimated from the Tauc plot, the conduction band maximum (CBM) of P25 and H-TiO_{2-x} should occur at approximately −0.98 and −1.35 eV, respectively. From a calculation of the energy band

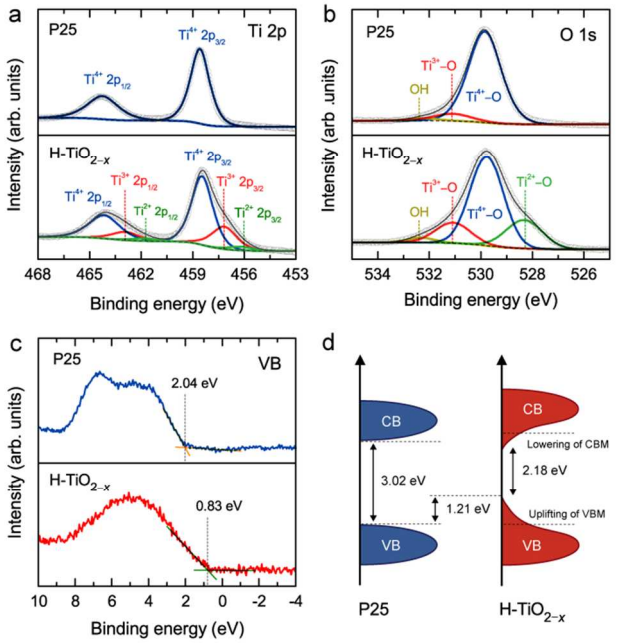

Fig. 5 High-resolution XPS spectra and peak deconvolutions of (a) Ti 2p and (b) O 1s regions for P25 and H-TiO_{2-x}. (c) XPS valence band spectra of P25 and H-TiO_{2-x}. (d) Schematic diagram illustrating density of state (DOS) of P25 and H-TiO_{2-x}.

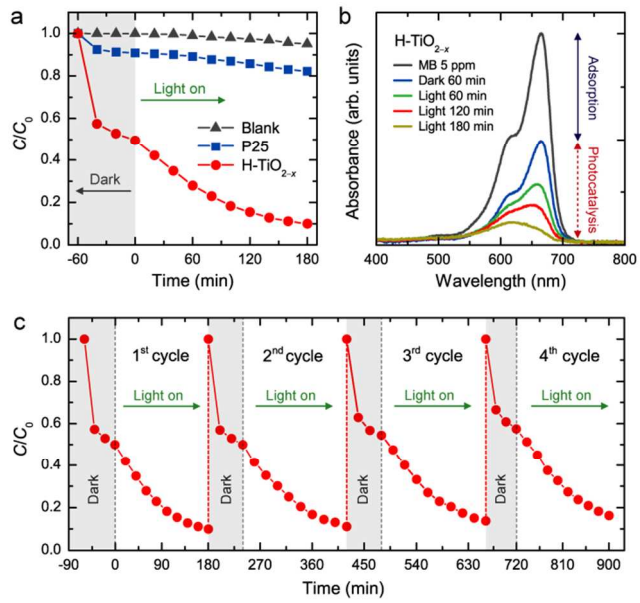

Fig. 6 (a) The change in relative concentration of MB (C/C_0) as a function of irradiation times under visible-light irradiation (λ > 420 nm, 150 W xenon lamp) in the absence and presence of P25 and H-TiO_{2-x}. (b) UV-visible absorption spectra of MB solution in the presence of H-TiO_{2-x} at different irradiation times. (c) Recycling photocatalytic activity of H-TiO_{2-x} toward MB degradation under visible-light irradiation.

structure by density functional theory (DFT) in literatures, the uplift of the VBM is likely due to the presence of structural disorder at the surface of H-TiO_{2-x}, while the localized states below the CBM arise from oxygen vacancies or Ti^{3+} sites.[17,29,34] The tailing effect on both the VBM and CBM of H-TiO_{2-x} would give rise to a substantial band gap narrowing (2.18 eV), thus leading to the improvement of photoresponse in the visible-light region. Based on the above results, the density of state (DOS) of P25 and H-TiO_{2-x} are schematically illustrated in Fig. 5d.

The photocatalytic activity of P25 and H-TiO_{2-x} was evaluated using the degradation of methylene blue (MB) dye solution (5 ppm) as a model reaction under visible-light irradiation (λ > 420 nm, 150 W Xenon lamp). More detailed information of the photocatalytic measurements is given in ESI†. A change in the characteristic absorption peak of MB at 664 nm was monitored at different irradiation times to determine the MB degradation (Fig. S7†). The relative concentrations of MB (C/C_0, where C and C_0 represent the concentration of MB during the reaction time and the initial concentration of MB, respectively) in the absence and presence of photocatalysts at different irradiation times are shown in Fig. 6a. Almost no degradation of MB is observed under visible-light irradiation in the absence of a photocatalyst, indicating that the self-degradation of MB is negligible. In dark conditions, about 51% of the MB molecules are adsorbed on the surface of H-TiO_{2-x}, while only 9% of the MB molecules are absorbed on the surface of P25. The difference in adsorption ability between P25 and H-TiO_{2-x} is reasonably well correlated with their surface area. Under visible-light irradiation for 180 min, the MB is almost completely degraded in the presence of H-TiO_{2-x} (90%), whereas it is degraded only by 18% in the presence of P25. Due to the significant adsorption ability of H-TiO_{2-x}, it is necessary to confirm that the MB dyes are photodegraded rather than adsorbed on the H-TiO_{2-x} surface. The MB solution in the presence of H-TiO_{2-x} can reach the adsorption equilibrium at least 60 min and remain nearly unchanged for 180 min under dark conditions (Fig. S8†). This is evidence that the MB degradation in the presence of H-TiO_{2-x} under visible-light irradiation mainly occurs due to the photocatalytic reaction rather than adsorption process. Furthermore, the reaction kinetic analysis of MB degradation for P25 and H-TiO_{2-x} was investigated (Fig. S9†). It is found that the MB photodegradation of both P25 and H-TiO_{2-x} is in agreement with the pseudo-first-order kinetic reaction. The pseudo-first-order rate constant of P25 and H-TiO_{2-x} is calculated to be 5.95×10^{-4} and 9.30×10^{-3} min^{-1}, respectively. This result indicates that the H-TiO_{2-x} exhibits higher visible-light photocatalytic activity for the MB degradation than P25. To confirm the stability of H-TiO_{2-x}, the photocatalytic activity of H-TiO_{2-x} was carried out multiple times. The recycling test reveals that the adsorption ability of H-TiO_{2-x} progressively decreases from 51% for the 1st cycle to 43% for 4th cycle (Fig. S7†), which may be due to the loss of its surface activity during cycling. The pseudo-first-order rate constant of H-TiO_{2-x} is retained up to 7.24×10^{-3} min^{-1} after recycling four times (Fig. S10†), indicating that H-TiO_{2-x} possesses good stability and recyclability.

On the basis of the above results, we can conclude that the superior photocatalytic activity of H-TiO_{2-x} is mainly attributed to the synergistic effect of several factors, which can be explained as follows. The H-TiO_{2-x} has a large surface area and accessible mesopores, which offer more active sites for photocatalytic reaction as well as favor mass exchange between MB molecules and photocatalytic degradation products over the H-TiO_{2-x} surface. Due to a narrow band gap (2.18 eV) and visible-light absorption of H-TiO_{2-x}, the electrons in the valence band (VB) can be excited to the conduction band (CB) under visible-light irradiation, resulting in the generation of the holes in VB. The photogenerated holes subsequently oxidize adsorbed water or surface hydroxide anions (OH^-) to yield hydroxyl radicals (•OH). On the other hand, the photogenerated electrons reduce the dissolved oxygen, first forming superoxide anion radicals ($•O_2^-$) and then yielding hydroperoxy radical ($HO_2•$) upon protonation, and finally •OH radicals. The formation of •OH radicals plays an essential role in the decomposition of MB over the surface of H-TiO_{2-x} under visible-light irradiation. In addition, oxygen vacancies and Ti^{i3+} sites existed on the surface of H-TiO_{2-x} can serve as electron and hole traps, respectively.[27,32] These can thus enhance the separation efficiency of photogenerated electron-hole pairs or suppress charge recombination (extend the lifetime of the charge carriers), leading to efficient visible-light photocatalytic activity toward MB degradation. The schematic diagram of the photodegradation of MB by H-TiO_{2-x} under visible-light irradiation is depicted in Fig. 7. Another important factor that should be considered here is the crystalline phase of H-TiO_{2-x}. The correlation between the crystalline phase of H-TiO_{2-x} and the photocatalytic activity is quite complicated and still unclear at present. However, we believe that an unusual phase mixture of

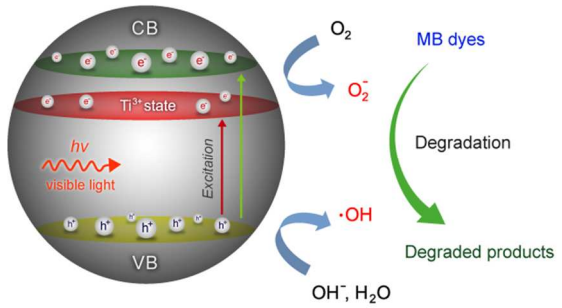

Fig. 7 Schematic diagram of the photodegradation of MB by H-TiO_{2-x} under visible-light irradiation.

different polymorphs in H-TiO_{2-x} (*i.e.*, anatase, rutile, and oxygen-deficient phases) under water plasma conditions may result in an increased photocatalytic activity compared with the pure phase.

In summary, a simple green method assisted by water plasma has been developed for the synthesis of stable-black H-TiO_{2-x} spheres at low temperature and atmospheric pressure. The *in situ* production of highly energetic OH and H species from water plasma play the essential roles for the oxidation and hydrogenation reactions of H-TiO_{2-x}. The synergistic effects of large accessible surface area, visible-light absorptions, and defect sites (*i.e.*, oxygen vacancies and Ti^{3+} ions) can promote the photocatalytic activity of H-TiO_{2-x} toward MB degradation under visible-light irradiation. We believe that this synthetic route can be potentially extended to the design and synthesis of various-defective metal-oxide particles for advanced photocatalysis and energy storage/conversion applications.

Acknowledgements

The authors gratefully thank Assoc. Prof. Nobuyuki Zettsu for fruitful discussions and valuable advices throughout this research.

Notes and references

[a]*Department of Materials Science and Engineering, Faculty of Engineering, Shibaura Institute of Technology, Tokyo 135-8548, Japan. E-mail: i036050@sic.shibaura-it.ac.jp, g.panomsuwan@gmail.com; Fax: +81-3-5859-8101; Tel: +81-3-5859-8115*

[b]*Social Innovation Design Center (SIDC), Institute of Innovation for Future Society, Nagoya University, Nagoya 464-8603, Japan.*

[c]*Department of Materials, Physics and Energy Engineering, Graduate School of Engineering, Nagoya University, Nagoya 464-8603, Japan.*

[d]*Green Mobility Collaborative Research Center, Nagoya University, Nagoya 464-8603, Japan.*

[e]*Core Research for Evolutional Science and Technology (CREST), Japan Science and Technology Agency (JST), Saitama 333-0012, Japan.*

† Electronic Supplementary Information (ESI) available: Experimental details, schamtic illustration of water-plasma-assisted synthesis, current-voltage waveform of water plasma, Tuac plot, particle-size distribution, N_2 adsorption-desorption isotherms, pore size ditribution, detailed deconvolution of high-resolution XPS Ti 2p and O1s spectra, photocatalytic activity measurement, UV-visible absorption spectra of MB at different irradiation times under visible-light irrradiation, pseudo-first-order plots of $-\ln(C/C_0)$ *versus* irradiation time of the MB degradation, XRD pattern and Raman spectrum of H-TiO_{2-x} after photocatalytic test, photodegradation of phenol solution by H-TiO_{2-x} under visible-light irradiation. See DOI: 10.1039/b000000x/

1 K. Hashimoto, H. Irei and A. Fujishima, *Jpn. J. Appl. Phys.*, 2005, **44**, 8269.
2 D. O. Scanlon, C. W. Dunnill, J. Buckeridge, S. A. Shevlin, A. J. Logsdail, S. M. Woodley, C. R. A. Catlow, M. J. Powell, R. G. Palgrave, I. P. Parkin, G. W. Watson, T. W. Keal, P. Sherwood, A. Walsh and A. A. Sokol, *Nat. Mater.*, 2013, **12**, 789.
3 T. L. Thompson and J. T. Tates, *Chem. Rev.*, 2006, **106**, 4428.
4 H. Li, X. Zhang, Y. Huo and J. Zhu, *Environ. Sci. Technol.*, 2007, **41**, 4410.
5 G. Liu, Y. Zhao, C. Sun, F. Li, G. Q. Lu and H. M. Cheng, *Angew. Chem. Int. Ed.*, 2008, **47**, 4516.
6 G. Yang, Z. Jiang, H. Shi, T. Xiao and Z. Yan, *J. Mater. Chem.*, 2010, **20**, 5301.
7 J. H. Pan, Z. Cai, Y. Yu and X. S. Zhao, *J. Mater. Chem.*, 2011, **21**, 11430.
8 A. Primo, A. Corma and H. Garcia, *Phys. Chem. Chem. Phys.*, 2011, **13**, 886.
9 T. Kamegawa, S. Matsuura and H. Yamashita, *Ang. Chem. Int. Ed.*, 2013, **52**, 916.
10 Z. Chen, L. Fang, W. Dong, F. Zheng, M. Shen and J. Wang, *J. Mater. Chem. A*, 2014, **2**, 824.
11 X. Pan and Y. J. Xu, *J. Phys. Chem. C*, 2013, **117**, 17996.
12 K. Woan, G. Pyrgiotakis and W. Sigmund, *Adv. Mater.*, 2009, **21**, 2233.
13 H. Zhang, X. Lu, Y. Li, Y. Wing and J. Li, *ACS Nano*, 2010, **4**, 380.
14 Z. D. Meng, L. Zhu, J. G. Choi, M. L. Chen and W. C. Oh, *J. Mater. Chem.*, 2011, **21**, 7596.
15 G. Tian, H. Fu, L. Jing, B. Xin and K. Pan, *J. Phys. Chem. C*, 2008, **112**, 3083.
16 B. Liu, L. M. Liu, X. F. Lang, H. Y. Wang, X. W. Lou and E. S. Aydil, *Energy Environ. Sci.*, 2014, **7**, 2592.
17 X. Chen, L. Liu, P. Y. Yu and S. S. Mao, *Science*, 2011, **331**, 746.
18 M. Kong, Y. Li, X. Chen, T. Tian, P. Fang, F. Zheng and X. Zhao, *J. Am. Chem. Soc.*, 2011, **133**, 16414.
19 J. Lu, Y. Dai and B. Huang, *Phys. Chem. Chem. Phys.*, 2011, **13**, 18063.
20 O. A. Syzgantseva, P. Gonzalez-Navarrete, M. Calatayud, S. Bromley and C. Minot, *J. Phys. Chem. C*, 2011, **115**, 15890.
21 G. Wang, H. Wang, Y. Ling, Y. Tang, X. Yang, R. C. Fitzmorris, C. Wang, J. Z. Zhang and Y. Li, *Nano Lett.*, 2011, **11**, 3026.
22 Z. Zheng, B. Huang, J. Lu, Z. Wang, X. Qin, X. Zhang, Y. Dai and M. H. Whangbo, *Chem. Commun.*, 2012, **48**, 5733.
23 S. Hoang, S. P. Berlund, N. T. Hahn, A. J. Bard and C. B. Mullins, *J. Am. Chem. Soc.*, 2012, **134**, 3669.
24 A. Naldoni, M. Allieta, S. Santangelo, M. Marelli, F. Fabbri, S. Cappelli, C. L. Bianchi, R. Psaro and V. D. Santo, *J. Am Chem. Soc.*, 2012, **134**, 7600.
25 W. Wei, N. Yaru, L. Chunhua, and X. Zhongzi, *RSC Adv.*, 2012, **2**, 8286.
26 T. Leshuk, R. Parviz, P. Everett, H. Krishnakumar, R. A. Varin and F. Gu, *ACS Appl. Mater. Interf.*, 2013, **5**, 1892.
27 X. Jiang, Y. Zhang, J. Jiang, Y. Rong, Y. Wang, Y. Wu and C. Pan, *J. Phys. Chem. C.*, 2012, **116**, 22619.
28 T. Xia and X. Chen, *J. Mater. Chem. A*, 2013, **1**, 2983.
29 Z. Wang, C. Yang, T. Lin, H. Yin, P. Chen, D. Wan, F. Xu, F. Huang, J. Lin, X. Xie and M. Jiang, *Adv. Func. Mater.*, 2013, **23**, 5444.
30 X. Yu, B. Kim and Y. K. Kim, *ACS Catal.*, 2013, **3**, 2479.
31 Z. Pei, L. Ding, H. Lin, S. Weng, Z. Zheng, Y. Hou and P. Liu, *J. Mater. Chem. A*, 2013, **1**, 10099.
32 J. Huo, Y. Hu, H. Jiang and C. Li, *Nanoscale*, 2014, **6**, 9078.
33 M. M. Khan, S. A. Ansari, D. Pradhan, M. O. Ansari, D. H. Han, J. Lee and M. H. Cho, *J. Mater. Chem. A*, 2014, **2**, 637.
34 Z. Wang, C. Yang, T. Lin, H. Yin, P. Chen, D. Wan, F. Xu, F. Huang, J. Lin, X. Xie and M. Jiang, *Energy Environ. Sci.*, 2013, **6**, 3007.
35 H. Tan, Z. Zhao, M. Niu, C. Mao, D. Cao, D. Cheng, P. Feng and Z. Sun, *Nanoscale*, 2014, **6**, 10216.
36 A. Starikovskiy, Y. Yang, Y. Cho, and A. Fridman, *Plasma Source Sci. Technol.*, 2011, **20**, 024003.
37 P. Bruggeman and D. C. Schram, *Plasma Sources Sci. Technol.*, 2010, **19**, 0045025.
38 E. Tatarova, F. M. Dias and C. M. Ferreira, *Int. J. Hydrogen Energy*, 2009, **34**, 9585.

39 Q. Chen, T. Kaneko, N. Matsuda and R. Hatakeyama, *Appl. Phys. Lett*., 2013, **102**, 244105.

40 Z. K. Zhang, M. L. Bai, D. Z. Guo, S. M. Hou and G. M. Zhang, *Chem. Commun*., 2011, **47**, 8439.

41 Z. Ding, G. Q. Lu and P. F. Greenfield, *J. Phys. Chem. B*, 2000, **104**, 4815.

42 Y. Sun, K. Yan, G. Wang, W. Guo and T. Ma, *J. Phys. Chem. C*, 2011, **115**, 12844.

43 J. Zhang, M. Li, Z. Feng, J. Chen and C. Li, *J. Phys. Chem. B*, 2006, **110**, 927.

44 P. M. Kumar, S. Badrinarayanan and M. Sastry, *Thin Solid Films*, 2000, **358**, 122.

45 C. N. Huang, J.-S. Bow, Y. Zheng, S.-Y. Chen, N. J. Ho and P. Shen, *Nanoscale Res. Lett*., 2010, **5**, 972.

46 S. J. Park, J. P. Lee, J. S. Jang, H. Rhu, H. Yu, B. Y. You, C. S. Kim, K. J. Kim, Y. J. Cho, S. Baik and W. Lee, *Nanotechnology*, 2013, **24**, 295202.